

Laboratory x-ray fluorescence tomography for high-resolution nanoparticle bio-imaging

Hans M. Hertz,* Jakob C. Larsson, Ulf Lundström, Daniel H. Larsson, and Carmen Vogt

Biomedical and X-ray Physics, Department of Applied Physics, KTH/Albanova, SE-10691 Stockholm, Sweden

*Corresponding author: hertz@biox.kth.se

Received February 5, 2014; revised April 4, 2014; accepted April 7, 2014;

posted April 8, 2014 (Doc. ID 205963); published April 30, 2014

We demonstrate that nanoparticle x-ray fluorescence computed tomography in mouse-sized objects can be performed with very high spatial resolution at acceptable dose and exposure times with a compact laboratory system. The method relies on the combination of the 24 keV line-emission from a high-brightness liquid-metal-jet x-ray source, pencil-beam-forming x-ray optics, photon-counting energy-dispersive detection, and carefully matched (Mo) nanoparticles. Phantom experiments and simulations show that the arrangement significantly reduces Compton background and allows 100 μm detail imaging at dose and exposure times compatible with small-animal experiments. The method provides a possible path to *in vivo* molecular x-ray imaging at sub-100 μm resolution in mice. © 2014 Optical Society of America

OCIS codes: (340.7440) X-ray imaging; (110.7440) X-ray imaging; (170.7440) X-ray imaging.

<http://dx.doi.org/10.1364/OL.39.002790>

X-ray fluorescence (XRF) from targeted nanoparticles (NPs) has potential to provide high-resolution 3D molecular x-ray bio-imaging. However, present laboratory XRF systems suffer from long exposure time and modest spatial resolution of >1 mm, also when operated with high NP concentration and at high radiation dose. In the present Letter, we show that a liquid-metal-jet source emitting a single-line high-brightness pencil beam in combination with energy dispersive detection will allow short-exposure-time sub-100 μm NP imaging at dose and NP concentration levels compatible with *in vivo* small-animal research. The major reason for the improvement is a significantly reduced Compton background level and the high-flux line-emitting source.

NP are investigated as alternatives to conventional absorption contrast agents for computed tomography (CT) [1–3]. Actively targeted NPs provide a path to molecular imaging and has been demonstrated in small-animal absorption CT for, e.g., lymph nodes (anti-CD4) or breast tumors (HER2) [4,5]. The typical NP dose is 0.1–1 mg Au/g tumor or organ after intravenous injection, corresponding to 10–100 Hounsfield units (HU). In these absorption experiments, objects down to one or a few mm were observable. This is consistent with our calculations of detectability (based on the “signal-known-exactly/background-known-exactly” task [6]): a few tens of HU are necessary to allow observation of a 1 mm object at 10 mGy dose in absorption imaging. Higher NP concentrations (up to 7 mg Au/g tumor) have been reached for radiation therapy experiments, and mice have been found to live more than a year after mg/g-level NP doses [7].

XRF has long been applied for CT [8], but early work with laboratory tubes resulted in painfully low signal-to-noise ratios (SNRs) and inadequate resolution. Synchrotron sources provide more flux and shorter exposure times [9] and are now extensively used for nano-tomography in the 10 keV regime [10]. However, the limited accessibility of these large facilities makes them less applicable for biomedical imaging. The last few years x-ray-tube-based fluorescence CT from metal NPs has been investigated in phantom studies, both experimen-

tally [11,12] and theoretically [13]. Typically the experiments show few mm resolution with 1%–2% metal NP concentration despite long exposure times and high dose. The major constraints are the low useful x-ray flux from the x-ray tube and the high Compton background resulting in a low SNR. The factors are to a significant extent due to the broadband nature and high energy of the source. Imaging of phosphor NPs instead (x-rays in, visible light out) [14] shows similar SNR and resolution limitations as in the XRF experiments.

Here we exploit the strong in-line emission at 24.1 keV photon energy from a liquid-metal-jet source for reduced exposure time and reduced background in small-animal metal-NP XRF. 24.1 keV is a suitable energy for mouse imaging, with a typical 50% transmission in 20 mm sized soft-tissue objects. Furthermore, it matches the absorption band of molybdenum. Mo is presently not used for NP imaging. Although much work remains before Mo NPs can be considered a safe *in vivo* contrast agent, its endogenous character [15] in combination with its low toxicity in *in vitro* studies (e.g., [16,17]) provides an encouraging starting point, motivating further investigations toward making this a biologically acceptable material. Furthermore, coating or other surface modifications can be employed for improving the biocompatibility of the NPs [18].

Figure 1 depicts the experimental arrangement. It consists of a liquid-metal-jet microfocus x-ray tube,

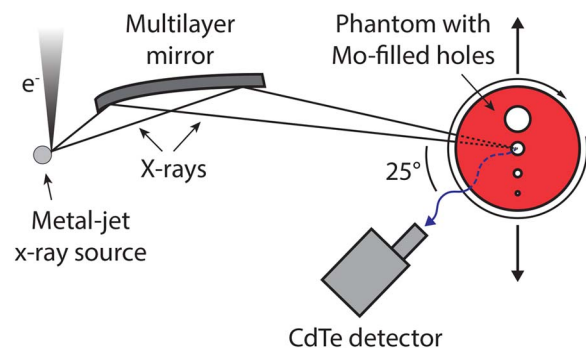


Fig. 1. Experimental arrangement.

multilayer optics for forming a single-line pencil beam, a phantom with Mo NP on a x - y - θ stage, and an energy-resolving photon-counting detector. The source is a prototype version of the D2 MetalJet by Excillum AB, Sweden, operated at 30 W e-beam power focused to a 8 μm spot on the GaInSn jet. The brightness in the emitted 24.1 keV In K_α line is $7 \times 10^8 \text{ ph/s} \times \text{mrad}^2 \times \text{mm}^2 \times \text{line}$). The double-bounce focusing multilayer Montel mirror is coated to reflect the 24.1 keV line. The input and output angles are 19.2 and 2.66 mrad, respectively. The measured focal spot is $125 \times 145 \mu\text{m}$ (FWHM), far from the sub-60 μm theoretically achievable due to figure errors in the mirror substrate of this first test mirror manufactured for this purpose. Thus the pencil beam has a diameter of $<150 \mu\text{m}$ over the full 20 mm diameter phantom. The 24.1 keV line emission flux in the beam is measured to $1.1 \times 10^6 \text{ ph/s}$ with two independent methods.

The phantoms consist of a 20 mm diameter polyethylene terephthalate (PET) plastic cylinder with four holes of different diameters (0.15, 0.3, 0.5, and 1.0 mm). PET was chosen since it has almost the same x-ray attenuation as soft tissue in the energy range used here. The 20 mm diameter is typical for a mouse. The Mo NP were obtained from US Research Nanomaterials Inc. Electron microscopy shows that the size distribution is broad (the mean diameter being 60 nm but the full distribution extending up to a μm) making them unsuitable for small-animal experiments but acceptable for the present proof-of-principle phantom experiment. They were suspended in glycerol to 0.5% concentration (by weight) and injected into the holes of the phantom. By the use of the viscous glycerol, sedimentation was minimized within the experimental time frames.

The $5 \times 5 \text{ mm}^2$ CdTe detector (Amptek X-123CdTe) is a single-photon-counting energy-dispersive detector. The measured bandwidth at the 17.4 keV Mo K_α fluorescence was 0.6 keV FWHM. It was placed 15 mm from the pencil-beam focus and at an angle of 25 deg to provide geometrical access and decrease Compton scattering. The full tomographic data sets were recorded by translating and rotating the phantom, providing path-integrated fluorescence measurements for each line. With 215 integrated line measurements per projection (100 μm steps) and 100 projections over 360 deg, the total exposure time was 6 h for the 0.5% Mo concentration and the SNRs demonstrated below.

Figure 2(a) shows the recorded fluorescence spectrum from the pencil beam traversing the full 20 mm diameter phantom and the 0.3 mm diameter hole filled with 0.5% Mo. The 17.4 keV Mo K_α fluorescence peak is clearly visible with a typical count rate of 20–25 ph/s within the 0.6 keV bandwidth. It is well separated from the Compton scattered photons, which peak at 22.5 keV. The 19.6 keV Mo K_β emission is not visible at these low Mo concentration levels. For comparison, the spectrum from a neighboring pencil beam, traversing no Mo inclusions, is given in the same figure. Here we typically measure $\sim 12 \text{ ph/s}$ background within the 0.6 keV bandwidth detection window of the Mo K_α line. The exposure time in both recordings was 100 s. Figure 2(b) depicts the corresponding Monte Carlo simulation [19] of the spectrum with the 0.3 mm/0.5% Mo inclusion, with and without smoothing

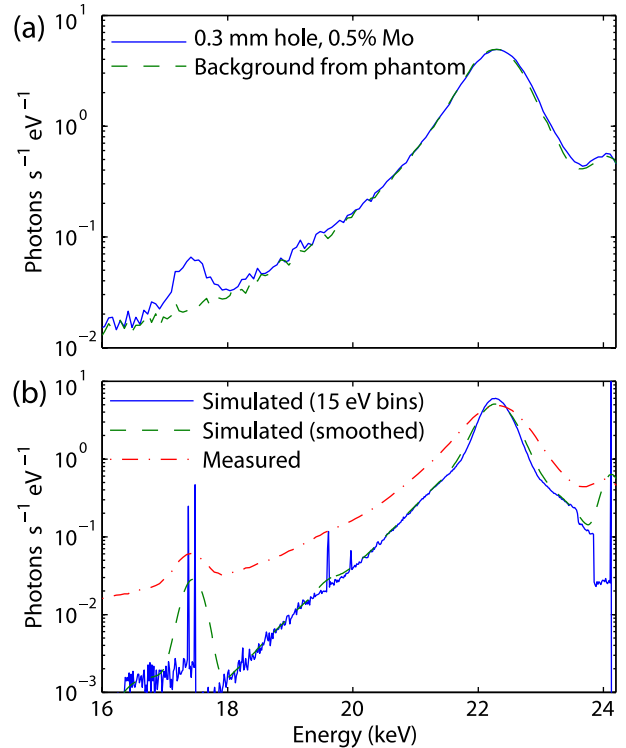


Fig. 2. (a) Experimentally recorded spectra from the phantom, with and without a 0.3 mm 0.5% Mo inclusion. (b) Monte Carlo simulation of the same situation at 0.015 and 0.6 keV bandwidth.

for the bandwidth of the detector (0.6 and 15 eV, respectively). The high-resolution spectrum resolves the 17.37 and 17.49 keV K_α double line. It is clear from the theoretical calculations that the major source of background noise at 17.4 keV is the low-energy wing of the Compton scattering from the phantom. Compton scattering from the Mo itself is small at these small-sized and low-concentration inclusions but can contribute to background at larger-diameter/higher-concentration inclusions. From Fig. 2, it is also clear that the SNR can be increased significantly with a narrower-bandwidth detector. Finally, in Fig. 2(b) the experimental and theoretical spectra are compared. The data sets agree well, although the experimental background is higher than the theoretical, possibly due to electronic detector noise.

Figure 3(a) shows the tomographic reconstructions of a phantom with 0.5% Mo in all four holes. The tomographic reconstruction was performed with a filtered back-projection algorithm on the 100 projections. Every projection consisted of 215 data points, where each point was calculated from the spectrally integrated in-band (0.6 keV bandwidth) photon numbers in the corresponding path-integrated fluorescence measurement. Here the measurement time was 1 s per integrated projection measurement. This is 50 \times times faster than previous work [11,12]. Figure 3(a) clearly demonstrates that 150 μm objects can be imaged with reasonable exposure times. The dose delivered was 700 mGy. This is on the high side for some small-animal experiments but can easily be reduced (cf. below).

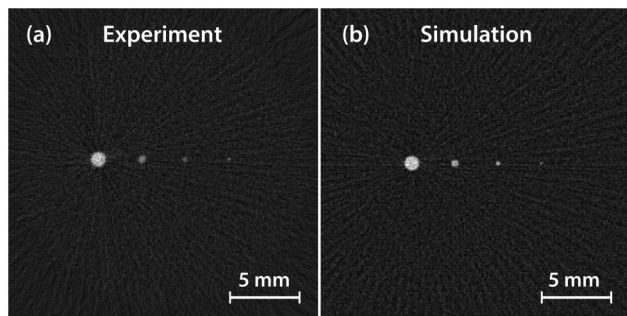


Fig. 3. (a) Tomographic reconstruction of the phantom with four small (1, 0.5, 0.3, and 0.15 mm diameter) inclusions with 0.5% Mo. (b) Simulation of the same experiment (b). Center of the image corresponds to the center of the phantom.

Figure 3(b) shows a simulation of the experiment. Here the quantitative total fluorescence signal was calculated, assuming 78% K-shell fluorescence yield [20] and a mass attenuation coefficient of $\mu/\rho = 4.28 \text{ kg/m}^2$ [21] out of which 83% is due to K-shell photo absorption. Attenuation in the PET phantom was also calculated with data from [21]. The correlation between experiments and simulations is excellent, the signal differing less than 5% for the 1 mm diameter inclusion. The difference is larger (few 10%) for the smaller inclusions, probably due to few-pixel statistics and/or NP sedimentation. From measurements of the observability [6], we conclude that the 1 and 0.15 mm diameter inclusions have $\text{SNR}^2 = 7000$ and $\text{SNR}^2 = 80$, respectively. Typically $\text{SNR}^2 = 25$ is sufficient to allow observation of a feature, giving room for a reduction of dose and exposure time.

For experiments on larger-diameter objects than 2 cm mice, the SNR^2 will be reduced due to increased absorption of both the incoming 24.1 keV pencil beam and the outgoing fluorescence radiation. Simulation of 4 cm diameter phantoms (e.g., small rats) with the same Mo inclusions and the same detector solid angle as above show that a 700 mGy dose results in $\text{SNR}^2 = 1050$, 65, and 11 for the 1, 0.3, and 0.15 mm diameter inclusions, respectively. Thus the 0.15 mm inclusion falls below the detection limit of $\text{SNR}^2 = 25$. To allow detection also of the smallest inclusion with the present experimental arrangement would require 41 h exposure time and 1600 mGy dose, i.e., considerably higher numbers than the 2 h and 220 mGy necessary for the same detectability on the 2 cm phantom.

Already the present proof-of-principle experimental arrangement illustrates the possibility of performing tomographic XRF NP imaging with significantly improved resolution and reduced exposure times and at a dose range relevant for small-animal imaging. The method is especially applicable for mouse-sized objects. Furthermore, the concept is scalable, and several improvements can be implemented in the near future: we are presently commissioning a new source operating at 400 W/8 μm spot size, increasing the $\text{In } K_\alpha$ flux $>10\times$ compared to what was used in the present measurements. Furthermore, the first-attempt mirror used here was far from optimal and will be improved both as regards reflectivity and figure errors. We hope to increase the reflectivity a factor five and reduce the figure errors so that a 50–70 μm

pencil beam can be produced. Finally, the detector area and, thus, solid angle, can be increased at least a factor 10 and potentially a factor 100. Furthermore, detectors can be positioned so that 360-deg scanning is unnecessary if object absorption allows it. With the new source, the improved mirror, and a $10\times$ larger detector, our calculations show that sub-100 μm resolution tomographic imaging of 0.5% (by weight in water) concentration Mo with $\text{SNR}^2 = 25$ can be performed with ~ 1 ms exposure time per integrated measurement in a 20 mm diameter object. Given 100 μm step size and 180 projections, this results in sub-minute exposure times. The total dose of such a tomographic recording is estimated to be <100 mGy, well within the acceptable range for many small-animal experiments [22]. Thus, the present method provides a path to whole-body *in vivo* small-animal molecular imaging with higher resolution than any existing method, already with the present state of technology. Additional improvements on the detector (area and bandwidth) will reduce both exposure times and dose even further, possibly more than an order of magnitude. Finally we note that further source improvements appear feasible, maybe to the several kW level, with a corresponding reduction in exposure times. The path to larger animals and clinical implementations involves several issues, which are beyond the scope of the present paper and, thus, will not be discussed here.

Finally we note that parallel measurements of the absorption of the incoming 24.1 keV beam can be used to improve the accuracy of the reconstruction by weighting the fluorescence tomographic map with the absorption tomographic map. This extra information comes at a no dose expense and may become especially important in real small-animal samples where bone absorption will need to be compensated for.

The authors gratefully acknowledge the discussions with Anna Burvall, Tunhe Zhou, and Muhammet Toprak and the loan of the mirror from Incoatec GmbH and Excillum AB. This project was financed by the Wallenberg Foundation and the Swedish Research Council.

References

1. J. F. Hainfeld, D. N. Slatkin, T. M. Focella, and H. M. Smilowitz, *Br. J. Radiol.* **79**, 248 (2006).
2. O. Rabin, J. M. Perez, J. Grimm, G. Wojtkiewicz, and R. Weissleder, *Nat. Mater.* **5**, 118 (2006).
3. M. Shilo, T. Reuveni, M. Motiei, and R. Popovtzer, *Nanomedicine* **7**, 257 (2012).
4. W. Eck, A. I. Nicholson, H. Zentgraf, W. Semmler, and S. Bartling, *Nano Lett.* **10**, 2318 (2010).
5. J. F. Hainfeld, M. J. O'Conner, F. A. Dilmanian, D. N. Slatkin, D. N. Slatkin, and H. M. Smilowitz, *Br. J. Radiol.* **84**, 526 (2011).
6. U. Lundström, D. Larsson, A. Burvall, P. A. C. Takman, L. Scott, H. Brismar, and H. M. Hertz, *Phys. Med. Biol.* **57**, 2603 (2012).
7. J. F. Hainfeld, D. N. Slatkin, and H. M. Smilowitz, *Phys. Med. Biol.* **49**, N309 (2004).
8. R. Cesareo and S. Mascarenhas, *Nucl. Instrum. Methods Phys. Res.* **A277**, 669 (1989).
9. A. Simionovici, M. Chukalina, C. Schroer, M. Drakopoulos, A. Snigireva, I. Snigireva, B. Lengeler, K. Janssens, and F. Adams, *IEEE Trans. Nucl. Sci.* **47**, 2736 (2000).
10. see, e.g., www.aps.anl.gov.

11. S.-K. Cheong, B. L. Jones, A. K. Siddiqi, F. Liu, N. Manohar, and S. H. Cho, *Phys. Med. Biol.* **55**, 647 (2010).
12. B. L. Jones, N. Manohar, F. Reynoso, A. Karellas, and S. H. Cho, *Phys. Med. Biol.* **57**, N457 (2012).
13. M. Bazalova, Y. Kuang, G. Pratz, and L. Xing, *IEEE Trans Med. Imaging* **31**, 1620 (2012).
14. G. Pratz, C. M. Carpenter, C. Sun, R. P. Rao, and L. Xing, *Opt. Lett.* **35**, 3345 (2010).
15. G. Schwarz, R. R. Mendel, and M. W. Ribbe, *Nature* **460**, 839 (2009).
16. L. Braydich-Stolle, S. Hussain, J. J. Schlager, and M.-C. Hofmann, *Toxicol. Sci.* **88**, 412 (2005).
17. G. Hasegawa, M. Shimonaka, and Y. Ishihara, *J. Appl. Toxicol.* **32**, 72 (2012).
18. B. Pelaz, S. Jaber, D. Jimenez de Aberasturi, V. Wulf, T. Aida, J. M. de la Fuente, J. Feldmann, H. E. Gaub, L. Josephson, C. R. Kagan, N. A. Kotov, L. M. Liz-Marzán, H. Mattoussi, P. Mulvaney, C. B. Murray, A. L. Rogach, P. S. Weiss, I. Willner, and W. J. Parak, *ACS Nano* **6**, 8468 (2012).
19. J. Baró, J. Sempau, J. M. Fernández-Varea, and F. Salvat, *Nucl. Instrum. Methods Phys. Res. Sect. B* **100**, 31 (1995).
20. J. H. Hubbell, P. N. Trehan, N. Singh, B. Chand, D. Mehta, M. L. Garg, R. R. Garg, S. Singh, and S. Puri, *J. Phys. Chem. Ref. Data* **23**, 339 (1994).
21. J. H. Hubbell and S. M. Seltzer <http://www.nist.gov/pml/data/xraycoef/index.cfm>.
22. C. T. Badea, M. Drangova, D. W. Holdsworth, and G. A. Johnson, *Phys. Med. Biol.* **53**, R319 (2008).